ACS APPLIED MATERIALS & INTERFACES

www.acsami.org Research Article

Revealing 3D Morphological and Chemical Evolution Mechanisms of Metals in Molten Salt by Multimodal Microscopy

Arthur Ronne, Lingfeng He,* Dmitriy Dolzhnikov, Yi Xie, Mingyuan Ge, Phillip Halstenberg, Yachun Wang, Benjamin T. Manard, Xianghui Xiao, Wah-Keat Lee, Kotaro Sasaki, Sheng Dai, Shannon M. Mahurin,* and Yu-chen Karen Chen-Wiegart*

Cite This: *ACS Appl. Mater. Interfaces* 2020, 12, 17321−17333 Read Online

ACCESS | Metrics & More | Article Recommendations | Supporting Information

ABSTRACT: Growing interest in molten salts as effective high-temperature heat-transfer fluids for sustainable energy systems drives a critical need to fundamentally understand the interactions between metals and molten salts. This work utilizes the multimodal microscopy methods of synchrotron X-ray nanotomography and electron microscopy to investigate the 3D morphological and chemical evolution of two-model systems, pure nickel metal and Ni-20Cr binary alloy, in a representative molten salt ($KCl-MgCl_2$ 50−50 mol %, 800 °C). In both systems, unexpected shell-like structures formed because of the presence of more noble tungsten, suggesting a potential route of using Ni−W alloys for enhanced molten-salt corrosion resistance. The binary alloy Ni-20Cr developed a bicontinuous porous structure, reassembling functional porous metals manufactured by dealloying. This work elucidates better mechanistic understanding of corrosion in molten salts, which can contribute to the design of more reliable alloys for molten salt applications including next-generation nuclear and solar power plants and opens the possibility of using molten salts to fabricate functional porous materials.

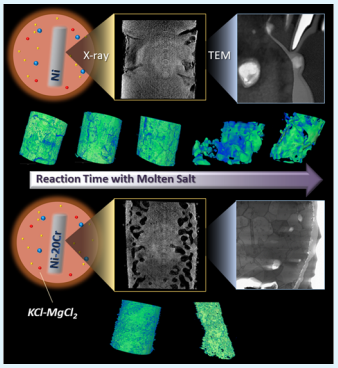

KEYWORDS: *chloride molten salt, high-temperature corrosion, Ni-based alloys, X-ray CT, TXM, molten salt corrosion, dealloying, multiscale imaging*

INTRODUCTION

Fundamental understanding of material behavior in extreme environments plays a critical role in advancing key technologies.[1−4] Specifically, the ability to manage materials evolution driven by thermal energies, and at times in conjunction with high chemical reactivities and/or radiation effects all in one environment, is crucial for sustainable energy industries such as safer, next-generation nuclear power plants and large-scale solar thermal power plants.[5] The need to transport high-temperature heat (>700 °C) is also prevalent in numerous other industries including oil refineries, shale oil processing facilities, and hydrogen production systems.[6] Among these technologies, a high-heat transfer fluid is essential to manage the heat produced or utilized in these systems; however, these applications bring great challenges to fundamentally understand and further manage or even design the interactions between the surrounding structural materials and the high-heat transfer fluid under these extreme environments for effective, economical, and safe operation.

Molten halide salts are one of the leading candidates for high-temperature heat transfer fluids because of their high boiling points, high specific heats, high thermal conductivities, and low vapor pressures.[7,8] Specifically, molten chloride salts have an advantage of being significantly lower in cost, having lower viscosities, and not having the potential to form hydrofluoric acid (HF) and thus being compatible with a wider range of materials.[6] This has led to increased interest in developing molten chloride systems for both next-generation solar and nuclear power plants. Molten LiCl-KCl has already been used for pyroprocessing of spent nuclear fuels.[9−11] Molten $KCl-MgCl_2$ specifically attracts interest because it has one of the highest volumetric heat capacities at 700 °C (0.46 cal/cm^3-°C) and one of the lowest costs among the chlorides.[6] In addition, the properties of the salt such as basicity can be changed by modifying the ratio of $MgCl_2$ to KCl. These properties have led to interest in $KCl-MgCl_2$ as a coolant for molten salt reactors and concentrated solar power. This has led to the increased study of $KCl-MgCl_2$ and related systems such as ternary salt $NaCl-KCl-MgCl_2$ in numerous recent works.[12] One of the leading challenges with molten chlorides, and molten halides in general, is their corrosivity in contact with structural alloys. At temperatures in excess of 700 °C, alloy reactions in chloride salts differ greatly from typical corrosion in aqueous solutions as they do not form a passivating oxide

Received: October 22, 2019
Accepted: March 26, 2020
Published: March 26, 2020

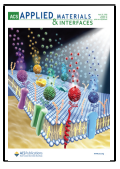

layer.[13−16] This fundamentally changes the corrosion mechanisms, and corrosion is driven instead by thermodynamic dissolution of component elements into the molten salt.[17−19] Constructed Ellingham diagrams show that the metal chlorination reactions to form Group I and II metal chlorides are more favored than the formation of transition metal chlorides,[20] potential corrosion products from structural alloys.

Nickel-based superalloys have been identified as one of the few classes of structural materials that can survive the harsh environment of a molten salt reactor (MSR), due to their relative thermodynamic stability and high-temperature creep strength.[15,21,22] Although pure Ni has greater thermodynamic stability, alloying elements are added to improve the high-temperature creep strength (Mo, Nb) and oxidation resistance (Cr).[23] However, as the redox potential for common alloying elements to form chloride salts decreases in the order W, Ni, Fe, Cr, Mg, K,[24] elements with lower redox potentials than Ni would lead to preferential dissolution of metals from the alloy into the molten salt.[25−27] With superalloys in the molten fluoride salt system, the corrosion rate increases with increasing Cr content, proceeding primarily through dealloying of Cr, which is more pronounced at grain boundaries[28−30] It has been shown that Cr will preferentially oxidize, corrode, and then form a porous network.[31,32] However, the nature of the porous network and fundamental mechanism governing its formation has not been discussed; such mechanistic understanding will be addressed in this work, which is crucial to predicting the corrosion rate, as well as designing alloys and molten salt systems to mitigate the issue.

Moreover, the purity of the salt as well as the overall reaction system have been shown to have the highest impact on the amount of corrosion observed;[33,34] impurities such as H_2O, or O_2 have been shown to greatly increase the rates of corrosion even in trace amounts.[35−37] On the role of metal impurities, Ye et al. have investigated the role of Fe^{3+} ions on corrosion in Hastelloy N and FLiNaK and observed iron oxidizing Cr and filling voids left by Cr.[33] The effect of metals with higher redox potentials remains to be studied further, as these metals may be present in molten salt system, either as fission products in MSRs or as contaminants. Tungsten is one such metal; it is widely used in numerous high-temperature applications and alloys and will be investigated in this study.

Understanding the metal−salt interaction is vital for understanding the degradation of structural alloys and for future materials design. Much work has been conducted on engineering Ni-based super alloys and stainless steels, but there is a need for addressing the fundamental scientific questions regarding how metals evolve in morphology and chemistry when exposed to molten salts.[33] Studies performed on simple, model systems of Ni and its binary alloys would help to reveal fundamental interaction between metals and molten salts, and hence Ni and the binary Ni-20Cr alloy are tested in this work. Cr was chosen as the alloying element, for it has been shown to exhibit preferential corrosion in alloys used for molten-salt applications.[38] Although prior studies in this field made significant progress in revealing the phenomena, they have largely relied upon macroscopic ex situ measurements, such as mass loss, to quantify corrosion.[39,40] This leaves a gap in the fundamental knowledge of the metal−molten salt interactions: Understanding the kinetics of alloy corrosion, namely, the morphological and chemical evolution as immersion time in molten salt progresses at multiple length-scales from micrometers, nanometers to atomic level, is critically needed for further development of new materials and corrosion mitigation methods.

This work thus takes a multimodal, multiscale imaging approach to study how the 3D morphology and chemistry of a pure metal and a binary alloy evolve in molten salt. Model systems Ni and Ni-20Cr (80 wt% Ni−20 wt% Cr) exposed to purified molten KCl-$MgCl_2$ (50:50 molar ratio) were systematically investigated as a function of reaction time at 800 °C. The relatively high temperature of 800 °C was chosen because it is a potential temperature for molten salt reactor operation.[41] Moreover, the high temperature should increase corrosion to enable observation of materials changes within the 100 h treatment time conducted in this study. The 3D morphological evolution of microwires in both systems were directly visualized via X-ray nanotomography using synchrotron-based transmission X-ray microscopy (TXM), and the same samples were then analyzed with transmission electron microscopy (TEM) to gain fundamental insight from the micrometer to nanometer scale. The 3D morphological characterization enabled by the nanotomography in TXM is crucial, as corrosion in an alloy is a 3D process where a 2D imaging technique would be limited. Overall, the work is pioneering in its observation of how pure metal and binary alloys evolve in 3D morphologically as they interact with the molten salt, and it sheds light on the corrosion mechanisms of molten salts for future materials design. The importance of metal ion impurities and defects, as well as several interplaying mechanisms including dissolution, dealloying, and faceting, shall be discussed.

RESULTS AND DISCUSSION

Single-Element Metal (Ni) 3D Morphological and Chemical Evolution in Molten Salt. Multiscale imaging was carried out by combining transmission X-ray microscopy with TEM. Ni microwires were vacuum sealed with a 50:50 molar ratio KCl-$MgCl_2$ mixture in quartz ampules and reacted at 800 °C for 1 to 100 h. An overview of the sample preparation procedure and setup can be found in Figure 1. The TEM analysis coupled with energy-dispersive X-ray spectroscopy (EDX) analysis mapping in scanning TEM (STEM) mode

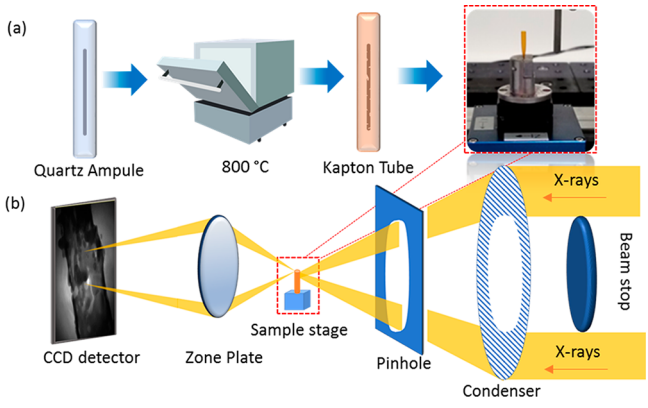

Figure 1. X-ray nanotomography characterization of metals reacted with molten salt: (a) An evacuated quartz ampule containing salt and wire is heated to 800 °C for the allotted time, then taken out and cooled. The ampule is then broken open, the salt is dissolved away with DI water and the wire is extracted and placed into a Kapton tube. This tube is then mounted at the FXI beamline. (b) FXI beamline setup.

https://dx.doi.org/10.1021/acsami.9b19099
ACS Appl. Mater. Interfaces 2020, 12, 17321−17333

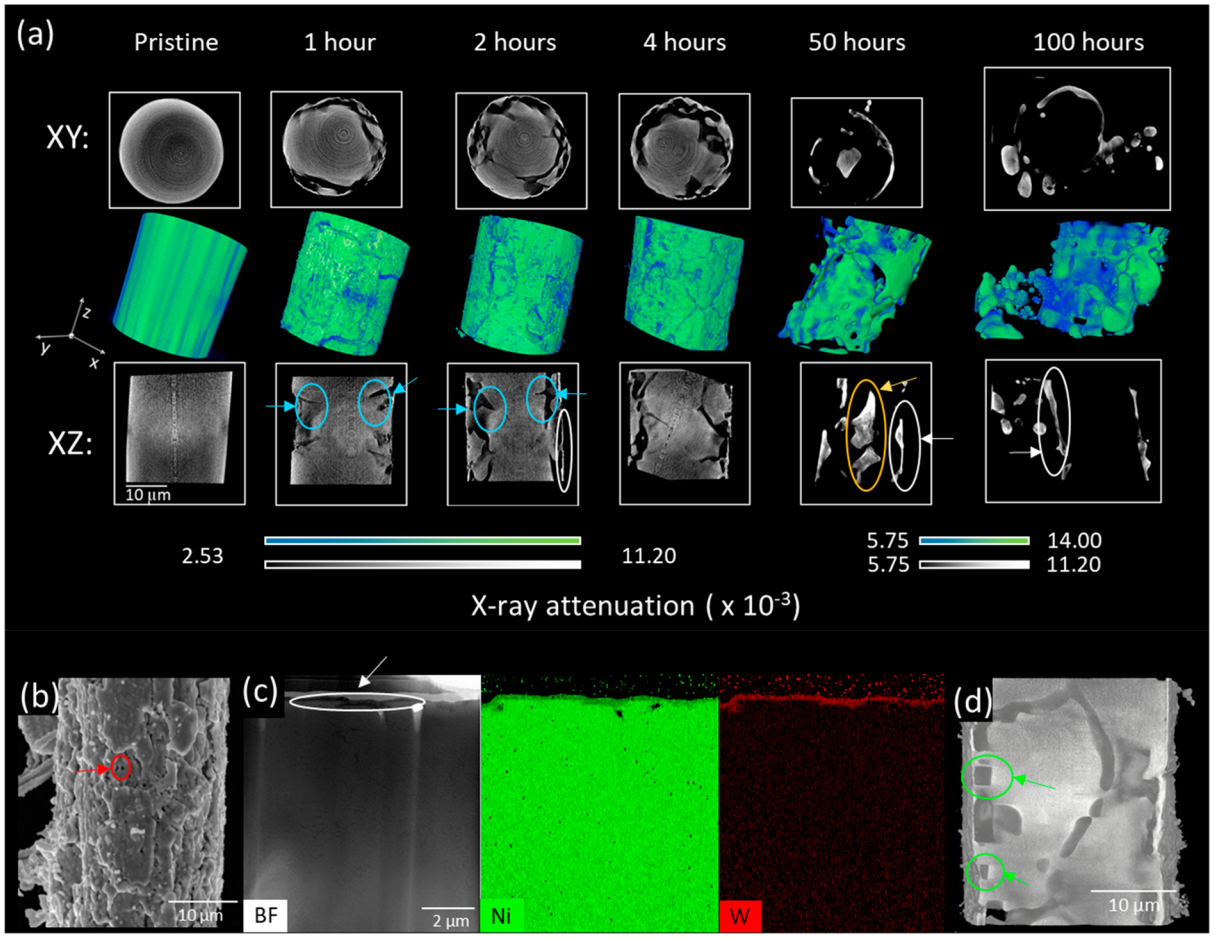

Figure 2. Overview of corrosion in Ni wire. (a) Reconstructed TXM images at above the Ni K-edge showing volume rendering, and pseudo cross-section images of $x-y$ and $x-z$ panes for 1−100 h. Blue circles show sharp features, white circles show the thin outer shell, and the yellow circle shows the inner core. (b) SEM image of the 1 h corroded Ni sample with the red circle showing small pores (c) TEM cross-section of the 1 h corroded sample with EDX mapping showing elemental distributions, with white circle showing the thin outer shell corresponding to the same features in a. (d) TXM 3D reconstruction shows faceting, as indicated by green circles, in the Ni microwire reacted in molten salt for 2 h.

provides even higher spatial resolution along with elemental distribution. Together, TXM and TEM with EDX are complementary techniques and when used together provide a more complete multimodal understanding of a structure and elemental distribution.[42]

The microstructures present in the pristine sample, including the grains and defects, as well as the chemical and elemental makeup, all have a significant impact on how the system evolves once interacting with the molten salt. Therefore, the pristine Ni microwire was characterized first. Characterization of the pristine Ni microwires by TXM, scanning electron microscope (SEM), STEM, and high-resolution TEM (HRTEM) techniques is presented in in the Figures S1 and S2. Overall, pristine Ni microwires exhibit no major defects and no visible oxide layer on the Ni wire's surface. Present on some regions of the surface of the Ni pristine microwires are small microcracks, harboring oxygen, typically a few nanometers in width and a couple hundred nanometers in length; this is important, as any oxygen present can greatly accelerate corrosion,[24] through either direct oxidation of Ni or reactions with the salt to produce species that can later attack Ni.

Figure 2 shows the 3D morphological evolution of the Ni microwire for molten salt immersion times of 1, 2, 4, 50, and 100 h. Additionally, Video S1 shows the full volume rendering rotations, and Videos S2 and S3 show the internal structure by displaying the $x-z$ and $x-y$ pseudo cross-sections. Over the first 1−4 h of immersion, the corrosion in the Ni wire starts with narrow, sharp features propagating directly into the wire in the r direction, then it evolves in the z direction as these crack-like features widen. These sharp features are circled in blue. In addition to the crack-like features, small holes are present throughout the surface, mostly in the 1 and 2 h corroded samples. Notably, a shell-like feature becomes visible at 2 h of immersion, as circled in white. The sharp, narrow features continue to widen until at 50 h of immersion only a thin surface shell and an inner core remain, circled in yellow. The edges of the remaining features in the 50 h sample are smoothed, likely due to curvature-driven coarsening at the elevated temperature. At 100 h, no inner core remains, but the surface shell persists and large surface growths have formed. Mosaic TXM images showing larger fields of view can be found in Figure S3.

The sharpness of the crack-like corrosion features in the TXM imagery alludes to corrosion operating through defects in the material, such as microcracks and grain boundaries, which both create a lower energy barrier to dissolution. Although the corrosion along the surface cracks and grain boundaries is consistent with the prediction, it cannot explain how a shell structure remained and slightly grew in thickness during the corrosion. Other mechanisms are suspected to play

https://dx.doi.org/10.1021/acsami.9b19099
ACS Appl. Mater. Interfaces 2020, 12, 17321−17333

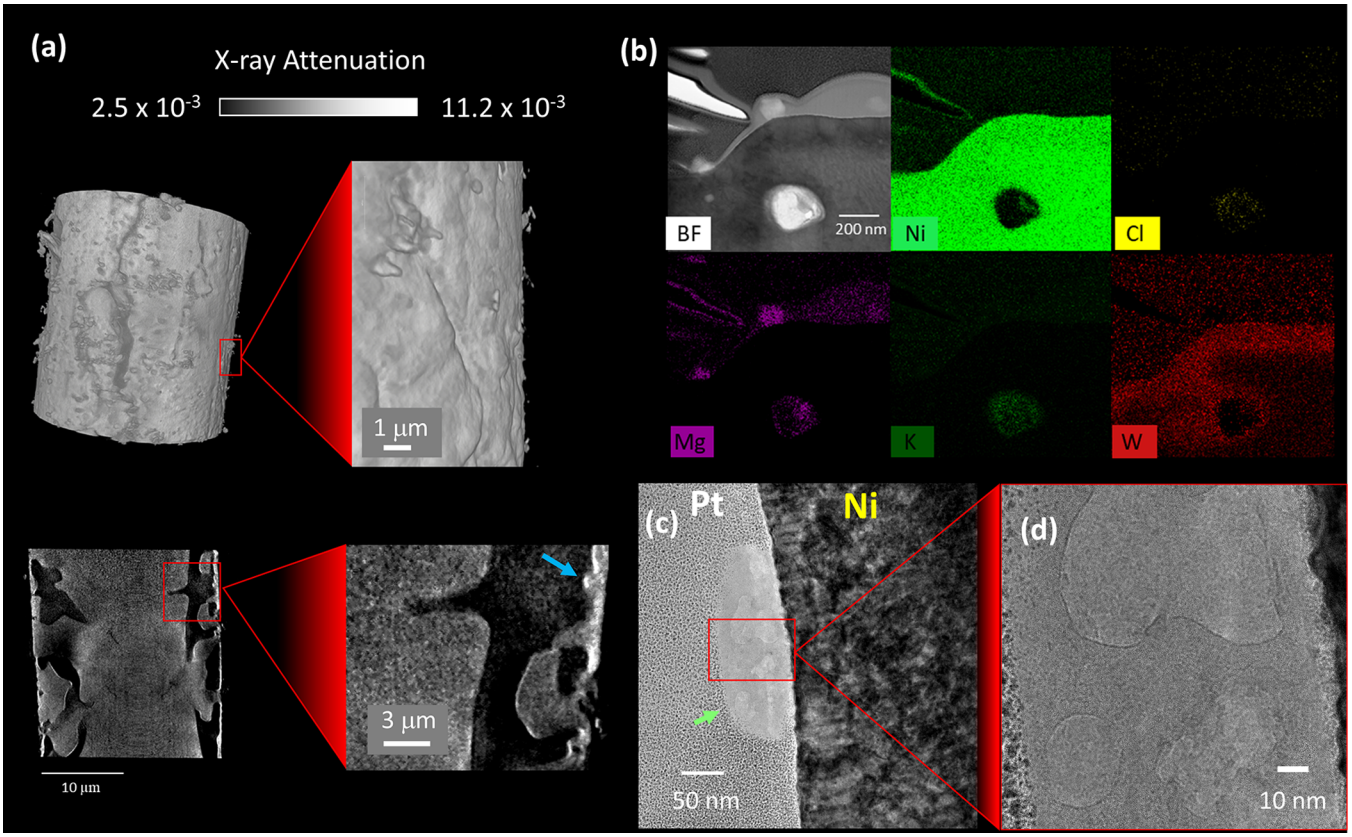

Figure 3. Surface of Ni microwire in the earlier stages of molten salt immersion. (a) TXM image at above Ni K-edge; from top left: volume rendering of 2 h corroded Ni, and a zoomed-in image of the surface showing various small growths. From bottom left: $x-z$ plane pseudo cross-section image of 2 h corroded Ni, and a zoomed-in image of the corroded pores. A blue arrow indicates the higher-attenuated region, likely containing W. (b) Bright-field TEM image of the surface with accompanying EDX, showing salt in the holes, and a W outer "shell" layer. (c) TEM image of the Ni surface showing an insoluble corrosion product, as indicated by a green arrow. (d) HRTEM image of the corrosion product present on the surface showing the lattice fringes.

a role here, and thus we have conducted further analysis and discussion to explain these mechanisms, as elaborated in the following sections. Figure 2b shows an SEM image of a 1 h corroded Ni wire sample. As seen in the SEM surface morphology, the sample has small holes, circled in red, and larger cracks, which are consistent with the images in the TXM.

Further STEM analysis showed that some metallic impurities present in the system significantly alter the 3D morphological evolution of the Ni microwire in the molten salt. Figure 2c is a bright-field STEM image with EDX elemental mapping for a Ni wire after 1 h of immersion. The EDX results show a thin layer of tungsten (W) forming on the surface of the wire. The presence of W is significant as a dissolved W cation, the speciation of this cation is not investigated by this work and this cation has several valence states; however, literature suggests W(IV) is the most likely valence state for the conditions studied[24,43,44] The W(IV) in the salts acts as a significant oxidizer, as it has a less negative redox potential (W/WCl_4) than that of Ni ($Ni/NiCl_2$) in this system.[24] This leads to the W oxidizing the Ni^0 to Ni^{2+} and the W^{4+} depositing onto the wire as W^0. This reaction drives Ni out of the system and into the salt but also creates a thin W layer on the surface of the wire. This overall reaction is

$$2WCl_4 + 4Ni \rightarrow 4NiCl_2 + 2W \quad (1)$$

We note that the redox reactions above will cease when all the W^{4+} ions in the system are expended for the cathodic reaction. From the TEM in Figure 2b it can be seen an approximately 200 nm thick layer of W on the Ni 1-h surface. Assuming this is both entirely W and a uniform coating of W this corresponds to 3.06 μg of W in the system, which could corrode 1.95 μg of Ni, corresponding to 4.46% of the wire. Therefore, corrosion of Ni induced by W reduction is not the dominant mechanism. The W could potentially come from the quartz ampules used in this work, as tungsten tooling is typically used for quartz manufacturing. The W was identified by high resolution inductively coupled plasma - mass spectrometry (ICP-MS) with the quartz ampules dissolved by HF, which showed 263 ± 5 ng of W per g in a quartz ampule sample. Additional ICP-MS analysis from the undissolved quartz ampule to confirm surface adsorbed species can be found in the Supporting Information. Note that this concentration is lower than the amount of W shown by EDX mapping in Figure 2c assuming the deposition of W is homogeneous and dense throughout the wires with 200 nm thickness. The source of Ti remains unclear as ICP-MS analysis on salt, quartz ampule and microwires indicated that the amount of Ti is beyond the detection limit. The very small amount of Ti likely contributed little to alter the corrosion pathway.

One possibility is the formation of Ni–W alloy as the two elements interdiffuse at the elevated temperature, based on the prediction of Ni–W phase diagram. This would suggest that a

https://dx.doi.org/10.1021/acsami.9b19099
ACS Appl. Mater. Interfaces 2020, 12, 17321–17333

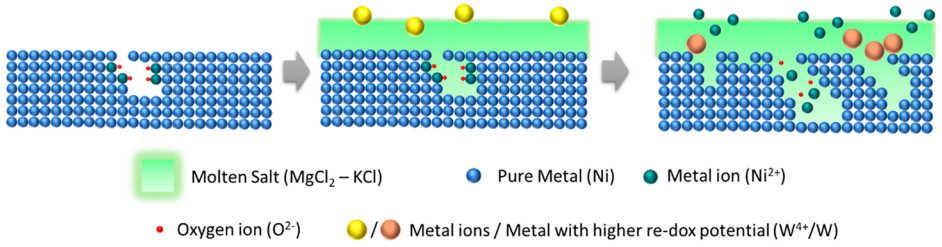

Figure 4. Proposed mechanism for Ni corrosion in the presence of small amount of W impurities, and oxygen present in the starting cracks.

Ni–W alloy, or surface W enrichment of Ni alloy, could be designed and used to significantly enhance the corrosion-resistance in molten salt applications. This corrosion resistance was also observed in the Ni-20Cr system as discussed in a following section.

Faceting is observed in the corroded Ni samples, as shown in Figure 2d. Figure S4a–c further display selected pseudocut views of x–z planes at three different locations in the 2 h immersed sample. Circled in red are square voids that may have been caused by either faceting or preferential corrosion along certain crystal orientations. Additionally, Videos S2 and S3 show these facets in samples at different time points and orientations. Faceting occurs because of the different lattice planes having differing surface energies, and thus rearrangement occurs along the planes with the lowest energy. Such processes generally occur at lower temperature, where the differences in surface energies of different crystallographic planes are more significant. Alternatively, preferential corrosion along specific lattice planes can also lead to similar microstructures.[32,33] Because of the lack of surface free energy data for metals in molten salt environments, the lattice plane orientations here are not known. Future work to investigate the faceting and obtain thermodynamic data on metal–molten salt interactions will be beneficial. However, it is believed that at high temperature (800 °C), even if there were preferential corrosion along different crystallographic planes, such microstructure would not be stable and would thus quickly coarsen and/or evolve into a more isotropic structure. Faceting during cooling was thus considered a more plausible mechanism to explain such morphology.

Near-Surface Morphological-Chemical Character of Ni Metal Reacted with Molten Salts. Figure 3 presents the elemental distribution and morphology of a 2 h treated Ni wire, and further highlights the sharpness of the features. The volume rendering surface (Figure 3a) shows the formation of slight surface growths, which may have been formed either while the system was at 800 °C, or less likely as the system cooled back down to room temperature. If formed while at the elevated temperature, these growths may be insoluble corrosion products, or deposition of W. If formed as the system cools the growths may be due to reverse reactions depositing previously corroded Ni, as chemical equilibria will change with temperature. The zoomed x–z pseudo cross-section highlights the sharp features in the nickel left by corrosion. The brighter region as indicated by a blue arrow on the surface may be due to the presence of W, which has greater X-ray attenuation at this energy.

Figure 3b shows a bright-field STEM image with EDX. The EDX identifies the presence of W on the surface and K, Mg, and Cl in the voids. The K, Mg, and Cl likely flow into the sample through the surface cracks. Figure 3c shows an insoluble corrosion product present on the surface of the Ni and the HRTEM image on the right shows the lattice fringes of the Ni and Pt. EDX spectra can be found in Figure S11. Figure S5 shows the X-ray Absorption Near-Edge Structure (XANES) of the Ni-K edge of the Ni sample after 100 h of immersion. The XANES spectra indicate that there are no oxidized Ni compounds in the wire or on the surface of the wire; Ni(0) was identified in the remainders of the Ni microwires as well as in the features as redeposited on the surface. The most likely corrosion pathway of Ni is oxidation to Ni(II). This Ni(II) may be present in the salt, but further detailed chemical analysis is needed to confirm the corrosion products in the salt.

Mechanisms of Single-Element Metal (Ni) Morphological Evolution. Both the presence of tungsten, as well as water and oxygen impurities likely contribute to the corrosion of the Ni as depicted in Figure 4. Although care was taken to avoid moisture and oxygen impurities during the preparation of the sample wires encapsulated in quartz ampules, very small amounts of O_2 and H_2O can inevitably be involved from residual impurities in the salts, the ampules, and the specimens; some are trapped in microcracks on the surfaces. The presence of O_2 and H_2O in $MgCl_2$ can generate HCl and Cl_2 via different mechanisms as proposed in the literature.[45,46] The amount of corrosion caused by any residual H_2O and O_2 was estimated to be higher than the amount caused by the presence of W alone (see the Supporting Information).

Under the low O_2 partial pressure in KCl-$MgCl_2$ at 800 °C, the NiO film cannot exist as an oxide[36] and dissolves away ($NiO \rightarrow Ni^{2+} + O^{2-}$) or reacts with Mg^{2+} ($NiO + Mg^{2+} \rightarrow Ni^{2+} + MgO$), thermodynamically the formation of MgO is significantly more favored than the formation of NiO.[47] Thus, a bare Ni surface is subject to the molten salt, leading to further propagation along the microcracks. Therefore, these microcracks grow through Ni dissolution, and concurrently W is plating onto the surface and oxidizing more Ni. This oxidized Ni is then carried away into the salt and complexes with the chloride. Surface redeposition of Ni as the system cools or deposition of W as the system is being corroded can explain the surface growths seen. Future *operando* work should be conducted to further understand the contribution between different processes to the 3D morphological evolution. Faceting or preferential corrosion of Ni system occurs as the (100) or (110) plane, likely to lower the overall surface energy of the system,[33] leading to square-like voids formed along the corrosion propagation front.

Binary Alloy (Ni-20Cr) 3D Morphological and Chemical Evolution in Molten Salt. Ni-20Cr microwires were subjected to the same treatment and analysis protocol as the Ni microwires.

Differing from the Ni wire, characterization of the pristine Ni-20Cr wire showed no surface cracks. However, some Ca impurities were found, and further discussion on the pristine characterization shown in Figure S6 can be found in the

https://dx.doi.org/10.1021/acsami.9b19099
ACS Appl. Mater. Interfaces 2020, 12, 17321–17333

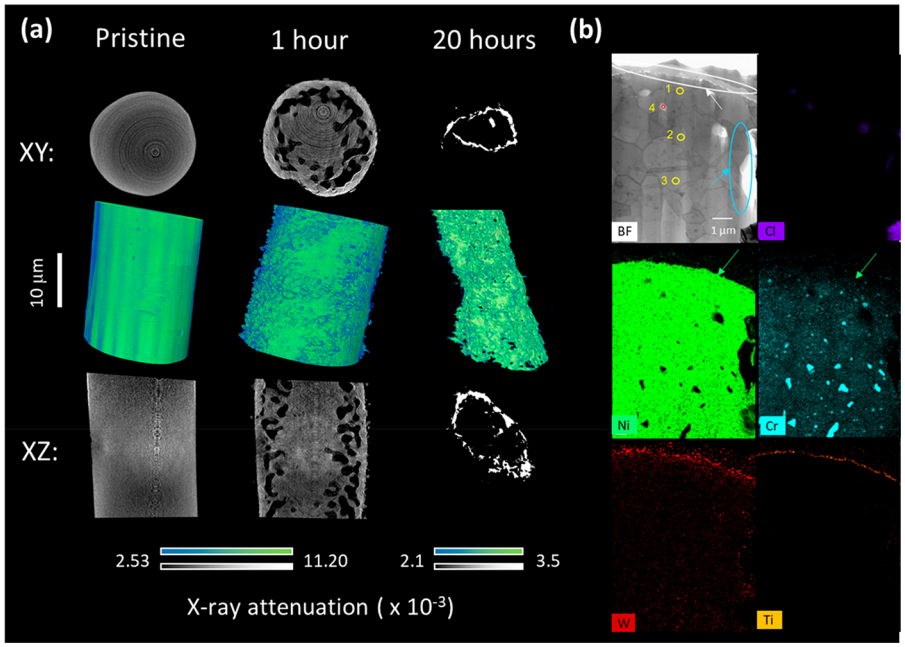

Figure 5. Overview of Ni-20Cr corrosion: (a) Reconstructed TXM images at above the Ni K-edge for 1 and 20 h after immersion. On top is $x-y$ pseudo cross-section, in the middle is the volume rendering, and on bottom is the $x-z$ pseudo cross-section. (b) TEM image of a transverse slice of Ni-20Cr after 1 h of immersion with EDX mapping and elemental composition at selected points. The shell is circled in white and a crack is circled in blue. Green arrows indicate the same location in Ni and Cr maps show Cr depletion.

Table 1. Elemental Composition from EDX Spectra of Selected Positions in Figure 5b

	elemental ratio (at %)								
position in Sample	Ni	Cr	Cl	Mg	K	W	Si	Ti	Pt
1	88.2	7.2				1.2	3.4		
2	84.1	12.1			0.1	1.1	2.0		0.6
3	81.6	16.6			0.1	0.6	1.1		
4	1.0		51.1	24.8	21.5		0.7	0.9	

supporting materials. As shown by the TXM images in Figure 5a, after 1 h of immersion, the Ni-20Cr wire forms a thick outer layer ~1 μm in size. Bicontinuous pores ~1−2 μm in feature size are present under this surface and extend approximately 5 μm into the wire, and the inner core of the wire is intact. As shown in Figure 5a, the 20 h treated Ni-20Cr sample has only an outer shell remaining, and the entirety of the inner material had been dissolved/corroded away, leaving a highly porous, thin surface shell ~0.5 μm thick. The starting diameter of the Ni-20Cr wire is 20 μm, and the 20 h sample at its widest has a diameter of 12−13 μm. This large reduction indicates that toward the later reaction stage the Ni has dissolved away as well and has participated in the corrosion process.

The porous structures observed here are akin to those observed in other molten salt studies,[32] but the mechanisms remain unclear. It is noteworthy that this 3D bicontinuous porous structure formed from treating Ni-20Cr for only 1 h in molten salt resembles the morphology formed by intentionally dealloying alloys to form porous metals for functional applications such as catalysts, fuel cells, biosensors, actuators and energy storage applications.[48−50] Those porous metals—some are nanoporous—were formed by dealloying using aqueous solution,[51−53] molten metals,[54−56] or solid-state metals[57,58] to drive selective dissolution. One or a few elements are dissolved from the precursor alloy, whereas the remaining element(s) rearrange, generally because of surface diffusion, to form a porous metal if the composition of the dissolving elements is above the percolation threshold and parting limit. We propose that a similar dealloying mechanism is responsible for the formation of the porous structure here in the Ni-20Cr system. The equilibrium potentials of the anodic reactions for Cr dissolution is shown below in eqs 2 and 3 at 800 °C are −1.58 and −2.0 V (vs Cl_2/Cl^-), respectively[24] and they are lower than that of $Ni/NiCl_2$, −1.3 V (vs Cl_2/Cl^-). Therefore, dissolution of Cr occurs preferentially compared with that of Ni.

$$Cr + 3Cl^- \rightarrow CrCl_3 + 3e^- \quad (2)$$

$$Cr + 2Cl^- \rightarrow CrCl_2 + 2e^- \quad (3)$$

As Cr being dissolved in the molten salt as promoted in the presence of impurities, Ni rearranged due to surface diffusion to reduce the energy due to the formation of adatoms, leading to further exposure of the Cr underneath the initial surface and causing the dealloying to continue.

Surprisingly, the wire did not form a complete porous network, but instead had a thick outer layer and a porous network underneath the surface "shell" after 1 h of reaction with the molten salt. This shows that differing mechanisms are playing a role here in addition to the dealloying mechanism. As shown by EDX mapping in Figure 5b a thin layer of W and Ti coats the surface of the Ni-20Cr wire after 1 h of immersion. The Ti redox potential is lower than W, Ni, and between Cr/

https://dx.doi.org/10.1021/acsami.9b19099
ACS Appl. Mater. Interfaces 2020, 12, 17321−17333

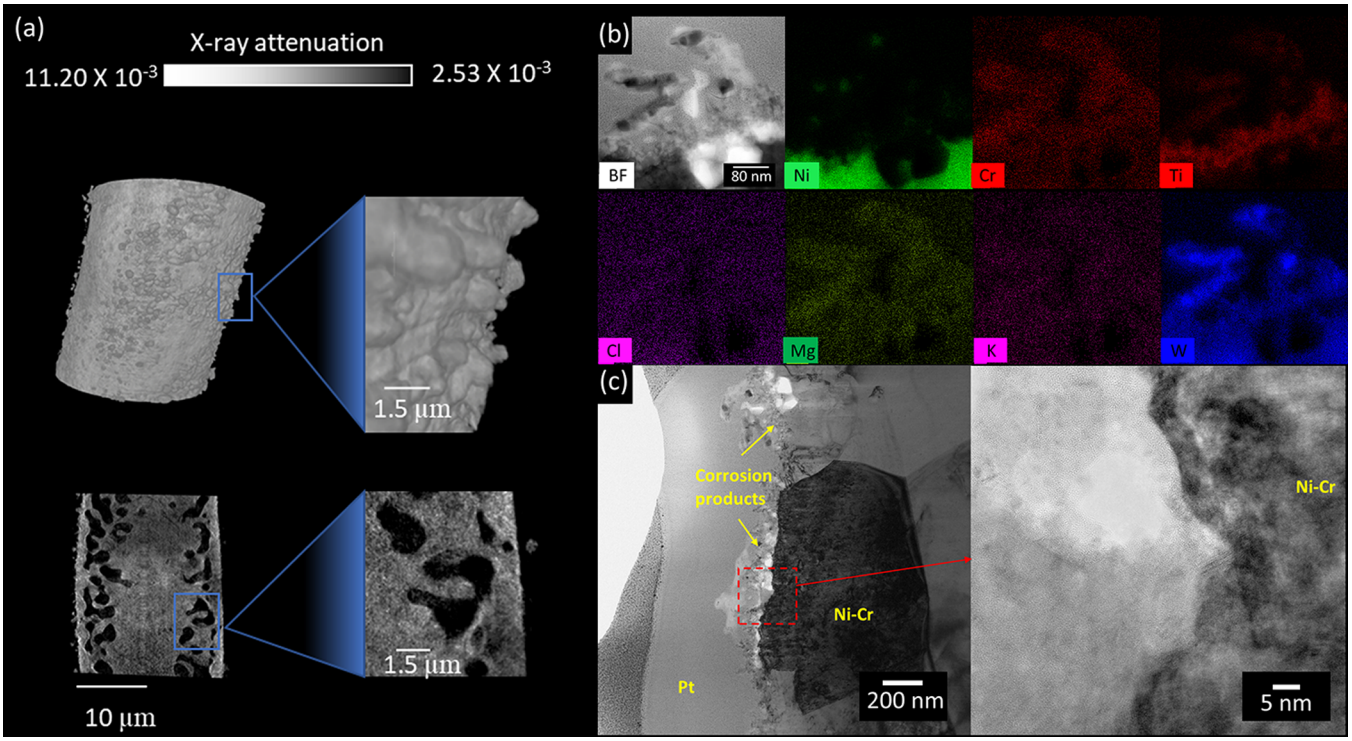

Figure 6. Surface of Ni-20Cr post-immersion. (a) TXM reconstructed image of the above Ni K-edge tomography. From top left: 3D volume rendering, surface of volume rendering. From bottom left: $x-z$ pseduo cross-section, zoomed in on pores of the $x-z$ pseduo cross-section.(b) STEM with EDX mapping of the surface protrusions present after 1 h of immersion. (c) TEM and higher zoomed TEM image showing the insoluble surface corrosion products present.

$CrCl_3$ and $Cr/CrCl_2$, so Ti can dissolve Cr to $CrCl_2$. The source of W and Ti is currently unknown, but, as in the case for the Ni wire, it is suspected to originate from the quartz ampule and diffuse into the salt at high temperatures, then react with the wire.

As seen in Figure 5b the Ni-20Cr system had preferential Cr depletion at the surface. The point EDX scans (Table 1) from point 1−3, from surface toward inner part of the microwire, showed 7.1, 12.2, and 16.6 at. % of Cr. Metal with the lowest redox potential in an alloy in molten salts will preferentially oxidize, and corrode into the salt.[24] The EDX results also showed that the more dense layer above the porous layer has a small amount of W (∼ 1 at. %) alloyed with Ni, confirming the hypothesis of Ni−W alloy formation as also discussed in the Ni system. A prior report showed improved corrosion resistance of W and Mo in engineering materials.[59] As this W addition seems to increase the corrosion resistance of the alloy significantly, further study can be conducted to analyze systematically the effects of W in Ni alloy either as an alloying element or via surface-enrichment treatment to enhance corrosion resistance.

Approximately 6 μm from the surface there are large Cr aggregates roughly 500 nm in size. As Cr leaches out from the surface a concentration gradient is created and more Cr diffuses toward the surface. As these diffusing Cr atoms encounter other Cr atoms, they coalesce and grow. The growth of Cr aggregates is thermodynamically favored due to lowering its free energy. Once these aggregates encounter the molten salt they will be corroded away as an entire block. The Cr aggregates are further seen in the below Ni K-edge TXM images shown in Figure S7. At an X-ray energy below the Ni K-edge (8.3 keV), Cr is more attenuating than Ni, so the bright spots on the 1-h reacted sample correspond to the Cr aggregates.

Figure 5b reveals the presence of salt in the voids formed during corrosion, through EDX elemental mapping of K, Mg, and Cl. There are multiple mechanisms by which this may have occurred. First, there may be small holes formed from surface dissolution in the outer layer which allow salt to flow in. Second, the K^+, Mg^{2+}, and Cl^- ion may diffuse through the metal lattice or grain boundaries and deposit in the voids as the sample cools down.

Near-Surface Morphological-Chemical Characters of Binary Alloy (Ni-20Cr) Reacted with Molten Salt. The thick outer surface of the 1-h immersed Ni-20Cr sample has characteristic rounded protrusions on its surface. This surface growth differs from the corrosion in Inconel observed by Manly et al., who showed corrosion evolving from the surface inward.[21] Shown in the above Ni K-edge pseudo cross-section in Figure 6a, the surface of the wire has a brighter, more attenuating section. This alludes to the presence of an element with a higher Z than Ni present in this area. The STEM/EDX of the top of an extruded feature shown in Figure 6b presents that this higher Z element is most likely W, and that the surface crust also contains Cr, Ti, Ni, and elements from the salt. The W is present on the immediate surface, the Ti and Ni are present in greater quantities underneath this structure, and the Cr has a depletion layer under this structure, previously highlighted in Figure 5b. These protrusions most likely form through both deposition of W, and formation of corrosion products on the surface.

Corrosion products are present on the surface of the 1 h immersed sample as well, and these are highlighted in Figure 6c. Note that these corrosion products are insoluble−any

https://dx.doi.org/10.1021/acsami.9b19099
ACS Appl. Mater. Interfaces 2020, 12, 17321−17333

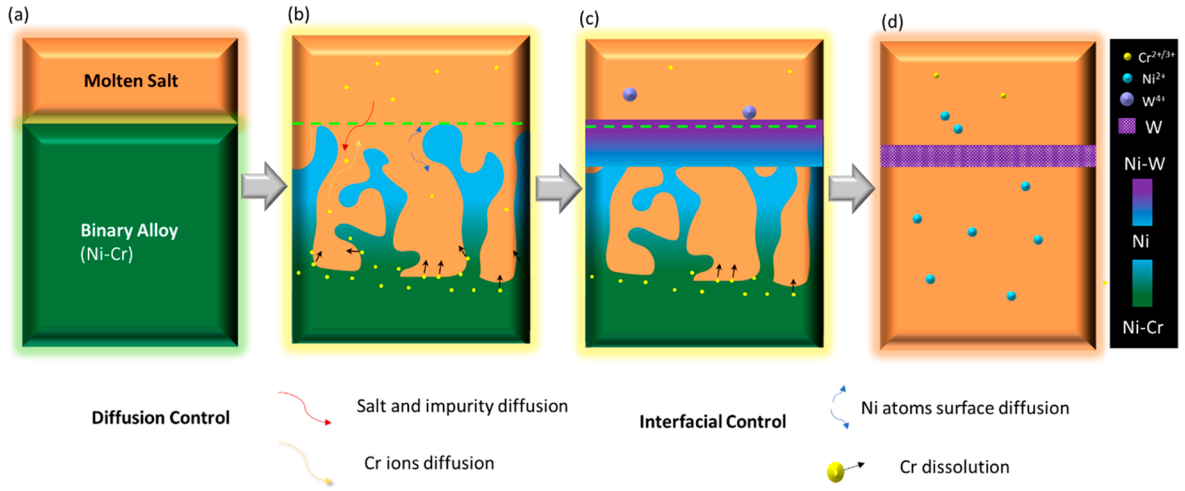

Figure 7. Proposed mechanism for binary alloy (Ni-20Cr) dealloying in molten salt in the presence of a noble element (W): (a) pristine state and (b) in a pure system where no surface deposition of other elements, a dissolution/dealloying only mechanism would result in a continuous dissolution of the element with lower redox potential (Cr) as indicated by black arrows, whereas the remaining element (Ni) would rearrange by surface diffusion (blue arrows), leading to further dealloying of the pristine alloy underneath. The morphology and topology of this process would largely depend on the composition and dealloying conditions. (c) When another element with higher redox potential is present (W), an additional surface deposition and potentially alloying with the undealloyed element (Ni) would from a layer on the surface, thereby altering the dealloying rate. (d) As all of the element with the lowest redox potential (Cr) is fully dissolved, the impurity-facilitated molten salt reaction starts to react with the undealloyed element (Ni), leaving the most noble element (W) as a shell of the structure.

soluble products would have been washed away during the DI water washing. These corrosion products may contain oxides, which most likely form because of the oxides introduced into the system from the thin oxide layer of the pristine sample, any oxygen contained in the salt, or perhaps after contact with water in the DI wash. See the Supporting Information for more discussion on possible oxides present from EDX results. Figure S9 shows the XANES of the Ni K-edge on the Ni-20Cr sample after 1 h of immersion. From the XANES spectra, we learn that all Ni in the alloy and on the surface is zero valent.

Mechanisms of Binary Alloy (Ni-20Cr) Morphological Evolution. The analogy of the dealloying mechanism in molten salts and in other systems as discussed above has several important implications: (1) Compositional effects: This porous structure will only form when the less noble element (Cr) composition is above the percolation threshold and parting limit; for FCC metal, the percolation threshold is ~20 at%, corresponding to ~18 wt% of Cr in Ni-Cr alloys.[60] Chang-Changing the composition of Ni alloy will directly influence the mechanisms and thereby the morphology and rate of its reaction with the molten salts. (2) Temperature effects: At the temperature used for this study, the bulk diffusion remains an order of magnitude slower than the surface diffusion. However, as the temperature increases or in other alloy systems with lower melting points, the bulk diffusion may start contributing to the process. Under such conditions, "inverse dendrite" formation as proposed by Sieradzki *et al.*[61] may also occur in molten salt dealloying systems, via a vacancy-mediated lattice diffusion mechanism.

This also leads to the question whether the dealloying in molten salt is interface-controlled instead of long-range diffusion control (Figure 7a-b). A future temperature-dependent study could be conducted to determine whether the phenomena occur at the interface, such as Cr dissolution and Ni surface diffusion, or the bulk diffusion such as diffusion through the porous network of molten salts ions inward or dissolved Cr ions outward are the rate-determining factors. Prior work has shown that free corrosion of Au−Ag in nitric acid up to several μm in depth is interface-controlled.[53]

Much remains to be unveiled in molten salt dealloying phenomena as the rates for the above competing mechanisms change when in molten salt environments. The presence of W and the simultaneous formation of the denser surface layer, likely Ni−W alloy, above the dealloying region (Figure 7c) likely inhibit both the long-range diffusion and interfacial reaction by locally increasing the dissolved ion concentration and thereby decreasing the driving forces for both events, but the quantitative relationship is yet to be determined. Additionally, the effects of having ions of a noble element, e.g., W, as impurities in the system ultimately leading to the dissolution of Ni with a porous shell as the remnants of the event (Figure 7d). Although there is a driving force for W to diffuse inward because of the concentration gradient and to form a diffusion couple with Ni-20Cr, at the immersion temperature used here, the bulk diffusion through the crystal lattice is significantly lower than surface diffusion or diffusion through the grain boundaries. The pores are therefore unlikely to be formed by the Kirkendall effect but rather the results of surface diffusion of Ni during the dealloying of Ni-20Cr.

Complications of the impurity-driven dissolution/corrosion process lead to a more complex picture of molten salt dealloying. Further work is required to quantitatively determine the controlling factors of both mechanisms as functions of reaction conditions, including the composition of the initial binary alloy, the concentration of additional metal ions with higher redox potentials, the reaction temperature and solubility. Moreover, although corrosion is detrimental for molten salt reactors, this dealloying phenomenon in molten salt can be utilized to purposely form porous metals that exhibit unique physical and chemical functionalities, creating another dimension of molten salt applications.

Future work on studying this morphological evolution quantitatively as a function of the reaction conditions including alloy composition, impurity, and temperature will provide

https://dx.doi.org/10.1021/acsami.9b19099
ACS Appl. Mater. Interfaces 2020, 12, 17321−17333

insights on the kinetics of these mechanisms—primarily dissolution facilitated by impurities, as well as morphological evolution facilitated by dealloying. With further understanding of alloy−molten salt interactions and expanding the pathways of the field to consider a broader range of materials science phenomena, future strategies and materials to mitigate and prevent materials degradation or even new functional materials by dealloying using molten salts can be designed for important future sustainable energy technologies.

CONCLUSION

In summary, a multimodal microscopy study of synchrotron X-ray nanotomography and transmission electron microscopy was conducted to reveal the 3D morphological and chemical evolution of pure metal and binary alloy in molten salt. Notably, both treated Ni and Ni-20Cr developed a hollow, shell-like structure with remnant Ni redeposition likely due to the presence of the W. This is consistent with the literature showing both the detrimental effects of noble metal impurities but also a the superior corrosion resistance of Ni−W in alloy design.[59,62,63]

The mechanisms governing the 3D morphological evolution in the pure metal and binary alloy differ significantly. The pure Ni metal likely corrodes through dissolution of Ni facilitated by small amounts of O impurities, as well as W oxidizing Ni. The presence of surface defects such as microcracks and grain boundaries provide lower-energy paths for the dissolution to proceed. In the binary Ni-20Cr system, corrosion progresses more rapidly than the pure Ni metal. As Cr preferentially dissolves in the molten salt from the Ni−Cr alloy, the remaining Ni rearranges into a bicontinuous network. Although the dissolution process is still likely facilitated by the impurities including oxygen and moisture based on the redox potentials of Ni, Cr, and KCl-$MgCl_2$ salt, the interconnected, bicontinuous porous metal network is characteristic, resembling a dealloying mechanism that has been studied in the recent years as a method to fabricate nano-/mesoporous metals for functional applications. This analogy has important implications including (1) this porous structure will only form when the less noble element composition is above the percolation threshold and parting limit, and (2) a temperature effect should be considered for the reaction at temperature sufficiently high in comparison to the melting point of the alloy, when bulk diffusion starts to contribute toward the system, in addition to the surface diffusion.

Overall, the work directly visualizes in 3D how metals evolve in molten salt, revealing structure including a bicontinuous network under percolation dealloying conditions and hollow structure formation under the presence of noble elements; the work also developed multiscale, multimodal microscopy characterization methodology for molten salt−metal systems to study the morphology and chemistry from nanometer to micrometer length scales.

METHODS

Salt Preparation. Salts used for experimentation were $MgCl_2$ and KCl. $MgCl_2$ was purified via fractional distillation starting from a commercial anhydrous salt and maintained in an air-free environment throughout the duration of experiments. Distillation is an effective method to remove both H_2O and MgO.[64] Any moisture present in the $MgCl_2$ at room temperature will usually be in the form of a hexahydrate. At high temperatures, the hydrate eventually decomposes to MgO and HCl. During the distillation process, the $MgCl_2$ was purified using a distillation chamber that consisted of a heated zone and a cold zone. The $MgCl_2$ was first loaded into one side of the distillation column which was heated to 925 °C while under a constant vacuum of 1×10^{-3} Torr. Over time, the pure $MgCl_2$ evaporated from the heated zone and condensed in the cold zone leaving any contaminants such as MgO in the heated zone. The vapor pressure of the MgO is too low at this temperature to diffuse to the cold zone. Once the distillation process finished, a valve to the condensed $MgCl_2$ was closed and the dried $MgCl_2$ was transferred to a glovebox without contacting air. The $MgCl_2$ was kept in the glovebox until being mixed. KCl was purchased as the 99.999% Suprapur reagent grade. The ampule containing the KCl was opened inside of an inert atmosphere drybox and was not removed for the duration of preparation process. Just before fusing the KCl-$MgCl_2$ mixtures, the distilled $MgCl_2$ and anhydrous KCl were melted to 825 °C and held under vacuum for 15 min. Heating under vacuum worked to remove any potential surface adsorbed water or gases that potentially penetrated the glovebox, sealed jar, and sealed vials that held the anhydrous salt before they were fused into the mixture and used for experimentation.

Molten-Salt Sample Treatment. Advances in X-ray microscopy have enabled computed tomography to be performed at the nanoscale and recently with the advances in synchrotron X-ray light source and instrumentation, such X-ray nanotomography can be performed within minutes.[65] The technique, known as TXM enables non-destructive three-dimensional characterization at sub-50 nm resolution with tens of microns field of view, and is well suited for studying the morphological evolution of alloys reacted with molten salt. TXM has been used with great success to study the 3D microstructure of a variety of systems including deformations in Al−Cu alloys,[66] growth of Cu nanowires,[67] and electrochemically driven phase transformations.[68] The large field of view in TXM allows information to be gained from a sizable volume of sample and allows both conformation of overall morphology and more statistical analysis.

Microwires were used in this study to enable the X-ray nanotomography analysis; the cylindrical shape is required to ensure a consistent X-ray attenuation from all imaging directions. The diameter is required to be on the order of ∼ 20 μm to ensure sufficient X-ray transmission, as well as a sample diameter smaller than the field of view for the best 3D reconstruction. Starting wires of Ni-20Cr (99.5% pure) with diameter 20 μm, and Ni wire (99.98% pure), diameter 25 μm were thus used for this study (Goodfellow, USA). Typical vendor analysis is available in the Supporting Information. The 20 at. % Cr was chosen here for the availability of such fine microwires as a model system in the work; fine wires with other compositions could be prepared via methods such as the Taylor wire technique.[69] Both types of wires were drawn through a diamond die, and annealing was not applied after the drawing. A certain level of the impurities as well as potential residual stresses are expected and will be addressed in the characterization and discussions.

For the corrosion test, each wire was cut to approximately 1 cm length and placed in a precleaned quartz ampule. Each ampule contained one wire. The purified salt was added, and the ampule was evacuated and flame-sealed. Literature data indicated that the vapor pressure for the KCl-$MgCl_2$ would be relatively low and thus significant volatilization would not be a major concern, especially with sealed ampules filled with the salts.[70,71] The quartz ampules containing the salt and wire were placed in a box furnace and heated to the target temperature of 800 °C at a ramp rate of approximately 20 °C/min. At each specified exposure time (e.g., 1, 2, 20 h, etc.), the appropriate ampule was removed and placed on a heat resistant block to rapidly cool to room temperature. Samples were then transferred while still evacuated in the ampules to Brookhaven National Laboratory for synchrotron analysis. Inductively coupled plasma-massspectrometry (ICP-MS) spectroscopic analysis was also conducted at ORNL on the quartz ampule; the quartz ampule was first dissolved in hydrofluoric acid, followed by ICP analysis.

https://dx.doi.org/10.1021/acsami.9b19099
ACS Appl. Mater. Interfaces 2020, 12, 17321−17333

Synchrotron TXM Experiment and Data Processing. *Nanotomography and X-ray Adsorption Near Edge Structure (XANES) Spectroscopic Imaging.* The synchrotron X-ray nanotomography and XANES spectroscopic imaging were conducted at the Full Field X-ray Imaging (FXI) beamline (18-ID) [45], at the National Synchrotron Light Source II (NSLS-II) at Brookhaven National Laboratory. The FXI beamline is equipped with a TXM and operates in the 6−10 keV energy range on a damping wiggler source, optimizing for fast nanotomography with the capability to conduct a full nanotomographic 3D scan as short as 1 min.[65]

To obtain a tomography image, we focused monochromatic X-rays onto the sample by a capillary condenser. The sample sits on an air-bearing rotary stage and was rotated from 0 to 180° at a speed of 1° per second; the images were collected in a fly scan mode, in which images were continuously recorded with a lens-coupled CCD detector with an exposure time ranging from 0.1 to 0.5 s. The detector used is the Andor Neo 5.5 camera with 2560 (H) × 2160 (V) pixels and 6.5 μm × 6.5 μm pixel size and the data were collected with binning of 2. The microscopy was setup such that the field view of the TXM was 41.6 μm (H) × 35.1 μm (V), with a pixel size of 32.5 nm. The data acquisition was conducted using BlueSky package, and the data management was handled by DataBroker package,[72] both developed in-house at NSLS-II. This procedure is repeated both at an energy slightly above and at an energy slightly below the X-ray absorption edge of the element of interest. In the case of Ni phase for both pure Ni and Ni-20Cr wires, the adsorption K-edge is at 8.333 keV, so the above-edge tomography was conducted at 8.4 keV and the below-edge one was conducted at 8.3 keV. The tomographic reconstruction was conducted using the standard filtered-back-projection in TomoPy, a Python-based tomographic reconstruction package developed at the Advanced Photon Source and implemented at the NSLS-II FXI beamline. All tomographic data were reconstructed with binning 2, yielding a voxel size of either 32.5 or 34.4 nm in the reconstructed volume.

The reconstructed 3D volume images were processed by cropping the central slices of ∼30 μm height where data has sufficient signal-to-noise ratio for good data quality using Fiji, a distributed version of freeware ImageJ[73] for further processing. 3D median filter was then applied in ImageJ to further reduce the noise level for visualization. The commercial software (Thermo Fisher Scientific, v9.4) was used for visualization of reconstructed data.

The XANES spectroscopic imaging was also conducted at the FXI beamline (18-ID) of NSLS-II. A series of TXM images were collected as a function of incident X-ray energy across specific absorption edges: Ni K-edge (8.333 keV) for both Ni and Ni-20Cr samples, and Cr K-edge (5.989 keV) for Ni-20Cr sample. Standard foil and powder samples of Ni foil, Cr foil, and nickel oxide power were also measured with the same conditions as the samples. Customized software developed in-house at Brookhaven National Laboratory was used for normalization and visualization of the XANES images to extra the XANES spectra data from the regions of interest (ROIs).

The vacuum-sealed quartz ampules as received from ORNL were scratched with a diamond pen and placed in a clean plastic bag for confinement during opening. The top part of the ampule was then broken open within the bag with a hammer. The bottom portion of the intact ampule, which contains solidified salt containing the corroded wire was then extracted and placed in DI water to dissolve the salt. Once the salt had dissolved completely, the wire was extracted and placed in a thin Kapton tube with diameter of 1 mm, which was then placed in an FXI sample holder for tomographic measurements.

TEM/STEM Sample Preparation and Analysis. The TEM samples were prepared by using a FEI Quanta 3D field-emission gun SEM-focused ion beam (FIB) system. The surface morphology of pristine and corrosion treated metal wires before TEM sample preparation was characterized in SEM/FIB. Platinum (Pt) coating was deposited to protect the surface before ion milling. TEM lamellae were created by coarse trenching 20 × 15 × 15 μm samples using the FIB. Samples were thinned down to around 100 nm in the FIB during a final milling step of 5 kV at 77 pA ion emission current. Gallium ion beam damage was cleaned with a final polish using 2 kV at 27 pA ion emission current. TEM lamellae were prepared along both longitudinal and transverse directions of pristine and corrosion treated Ni and Ni-20Cr wires. A FEI 200 kV Titan Themis 200 scanning transmission electron microscope (S/TEM) equipped with a Super-X EDX system was used for structure and composition analysis. The Cliff-Lorimer method was used for EDX elemental quantification in salt, metals, and impurities. The interface between metal and salt was visualized using HRTEM.

■ ASSOCIATED CONTENT

Supporting Information

The Supporting Information is available free of charge at https://pubs.acs.org/doi/10.1021/acsami.9b19099.

Information and further characterization of the pristine Ni and Ni-20Cr; TXM mosaic images and XANES spectra of treated Ni and Ni-20Cr; further images of faceting in treated Ni; information on the amount of Ni presumed to be corroded by the presence of O_2 and H_2O; discussion of Cr aggregation; EDX spectra at select points and atomic concentrations from Figure 3b and from treated Ni-20Cr; volume diffusion coefficient calculations of Ni, Cr, and W in Ni; ICP analysis of undissolved and HF-dissolved quartz samples, Ni and Ni-20Cr microwires, and KCl-$MgCl_2$ salt mixture; vendor certification of microwires composition (PDF)

Video S1 showing all above Ni-edge Ni-only volume renderings from Figure 2 (MP4)

Video S2 showing $x-z$ pseudo cross-section sequences from Figure 2 (MP4)

Video S3 showing $x-y$ pseudo cross-section sequences from Figure 2 (MP4)

Video S4 showing all above Ni-edge Ni-20Cr volume renderings from Figure 5 (MP4)

Video S5 showing $x-z$ pseudo cross-section sequences from Figure 5 (MP4)

Video S6 showing $x-y$ pseudo cross-section sequences from Figure 5 (MP4)

■ AUTHOR INFORMATION

Corresponding Authors

Yu-chen Karen Chen-Wiegart − *Department of Materials Science and Chemical Engineering, Stony Brook University, Stony Brook, New York 11794, United States; National Synchrotron Light Source II, Brookhaven National Laboratory, Upton, New York 11973, United States;* orcid.org/0000-0003-4445-2159; Email: Karen.Chen-Wiegart@stonybrook.edu

Shannon M. Mahurin − *Chemical Sciences Division, Oak Ridge National Laboratory, Oak Ridge, Tennessee 37830, United States;* orcid.org/0000-0003-3792-1631; Email: mahurinsm@ornl.gov

Lingfeng He − *Materials and Fuels Complex, Idaho National Laboratory, Idaho Falls, Idaho 83415, United States;* Email: lingfeng.he@inl.gov

Authors

Arthur Ronne − *Department of Materials Science and Chemical Engineering, Stony Brook University, Stony Brook, New York 11794, United States;* orcid.org/0000-0001-7507-0757

Dmitriy Dolzhnikov − *Chemical Sciences Division, Oak Ridge National Laboratory, Oak Ridge, Tennessee 37830, United States*

Yi Xie − *Materials and Fuels Complex, Idaho National Laboratory, Idaho Falls, Idaho 83415, United States*
Mingyuan Ge − *National Synchrotron Light Source II, Brookhaven National Laboratory, Upton, New York 11973, United States*
Phillip Halstenberg − *Chemical Sciences Division, Oak Ridge National Laboratory, Oak Ridge, Tennessee 37830, United States;* orcid.org/0000-0002-6030-4503
Yachun Wang − *Materials and Fuels Complex, Idaho National Laboratory, Idaho Falls, Idaho 83415, United States*
Benjamin T. Manard − *Chemical Sciences Division, Oak Ridge National Laboratory, Oak Ridge, Tennessee 37830, United States;* orcid.org/0000-0002-0740-0627
Xianghui Xiao − *National Synchrotron Light Source II, Brookhaven National Laboratory, Upton, New York 11973, United States*
Wah-Keat Lee − *National Synchrotron Light Source II, Brookhaven National Laboratory, Upton, New York 11973, United States*
Kotaro Sasaki − *Chemistry Division, Brookhaven National Laboratory, Upton, New York 11973, United States;* orcid.org/0000-0003-2474-8323
Sheng Dai − *Chemical Sciences Division, Oak Ridge National Laboratory, Oak Ridge, Tennessee 37830, United States;* orcid.org/0000-0002-8046-3931

Complete contact information is available at: https://pubs.acs.org/10.1021/acsami.9b19099

Author Contributions

Y.-c.K.C.-W., S.M.M., L.H., and S.D. developed the research idea. D.D. and P.H. prepared the high-purity salts under the supervision of S.M.M. and S.D. S.M.M. performed the high-temperature corrosion tests. Y.-c.K.C.-.W wrote user proposals for the use of the FXI beamline at NSLS-II and equipment at CFN. M.G. provided guidance on the FXI sample mounting method. A.R. conducted further sample preparation and mounting for the FXI experiment with input from D.D. and S.M.M., under the supervision of Y.-c.K.C.-W. W.-K.L., M.G., and X.X. designed and commissioned the FXI beamline; M.G. and X.X. set up the FXI beamline for the experiment and provided support during the experiment. A.R. and Y.-c.K.C.-W. performed the FXI experiment with the support from group members. M.G. wrote the software at FXI for data processing of tomography and XANES imaging. A.R. analyzed the X-ray nanotomography data under the guidance of Y.-c.K.C.-W. Y.W. prepared TEM samples and collected SEM images. L.F. performed TEM/STEM/EDS characterization and data analysis. Y.X. analyzed TEM/EDS data and interpreted the data for reaction mechanisms. B.T.M. conducted ICP analysis. A.R., Y.-c.K.C.-W., S.M.M., L.H., Y.X., D.D., and P.H. discussed and interpreted the results. K.S. calculated voltage potentials and provided further interpretation on the reaction mechanisms. A.R. wrote the manuscript and designed the figures under the guidance of Y.-c.K.C.-W., with inputs from all coauthors.

Notes

The authors declare no competing financial interest.

■ ACKNOWLEDGMENTS

This work was supported as part of the Molten Salts in Extreme Environments (MSEE) Energy Frontier Research Center, funded by the U.S. Department of Energy, Office of Science, Basic Energy Sciences. BNL, INL, and ORNL are operated under DOE contracts DE-SC0012704, DE-AC07-05ID14517, and DE-AC05-00OR22725, respectively. Work at Stony Brook University was supported by MSEE through a subcontract from BNL. This research used resources and the Full Field X-ray Imaging (FXI, 18-ID) beamline of the National Synchrotron Light Source II, a U.S. Department of Energy (DOE) Office of Science User Facility operated for the DOE Office of Science by Brookhaven National Laboratory under Contract DE-SC0012704. This research used resources of the Center for Functional Nanomaterials, which is a U.S. DOE Office of Science Facility, at Brookhaven National Laboratory under Contract DE-SC0012704. The authors acknowledge the support from CFN staff clean room access and training, and SEM training was provided by Gwen Wright. Chen-Wiegart group members are acknowledged for conducting the FXI beamtime experiment together and assisting with preliminary analysis: Cheng-Hung Lin, Xiaoyang Liu, Lijie Zou, and Chonghang Zhao. The authors acknowledge the assistance with sample and setup preparation from Bobby Layne.

■ REFERENCES

(1) Johnson, T.; Gates, T. High temperature polyimide materials in extreme temperature environments. In *19th AIAA Applied Aerodynamics Conference*; American Institute of Aeronautics and Astronautics: Reston, VA, 2001; p 1214.
(2) Fahrenholtz, W. G.; Hilmas, G. E. Ultra-high temperature ceramics: materials for extreme environments. *Scr. Mater.* **2017**, *129*, 94−99.
(3) Del Castillo, L.; Schatzel, D. V.; Tudryn, C.; Hatake, T.; Chen, Y.; Mojarradi, M.; Kolawa, E. Extreme environment electronic packaging for Venus and Mars landed missions. In *Proceedings of the 4th International Planetary Probe Workshop*, 2006.
(4) Sidhu, T.; Prakash, S.; Agrawal, R. Hot corrosion behaviour of HVOF-sprayed NiCrBSi coatings on Ni-and Fe-based superalloys in Na2SO4−60% V2O5 environment at 900° C. *Acta Mater.* **2006**, *54* (3), 773−784.
(5) Misra, A. K.; Whittenberger, J. D. Fluoride salts and container materials for thermal energy storage applications in the temperature range 973−1400 K. In *22nd Intersociety Energy Conversion Engineering Conference*; American Institute of Aeronautics and Astronautics: Reston, VA, 1987; p 9226.
(6) Williams, D. *Assessment of Candidate Molten Salt Coolants for the Ngnp/Nhi Heat-Transfer Loop*; Oak Ridge National Laboratory: Oak Ridge, TN, 2006.
(7) Sridharan, K.; Allen, T.; Anderson, M.; Simpson, M. *Thermal properties of LiCl-KCl molten salt for nuclear waste separation*; Report OSTIID 1058922 ; International Atomic Energy Agency: Vienna, Austria, 2012.
(8) Sohal, M. S.; Ebner, M. A.; Sabharwall, P.; Sharpe, P. *Engineering database of liquid salt thermophysical and thermochemical properties*; Report INL/EXT-10-18297 ; U.S. Department of Energy Office of Scientific and Technical Information: Oak Ridge, TN, 2010.
(9) Inoue, T.; Koch, L. Development of pyroprocessing and its future direction. *Nucl. Eng. Technol.* **2008**, *40* (3), 183−190.
(10) Merwin, A.; Phillips, W. C.; Williamson, M. A.; Willit, J. L.; Motsegood, P. N.; Chidambaram, D. Presence of Li clusters in molten LiCl-Li. *Sci. Rep.* **2016**, *6*, 25435.
(11) Yoo, J.-H.; Seo, C.-S.; Kim, E.-H.; Lee, H.-S. A conceptual study of pyroprocessing for recovering actinides from spent oxide fuels. *Nucl. Eng. Technol.* **2008**, *40* (7), 581−592.
(12) Polimeni, S.; Binotti, M.; Moretti, L.; Manzolini, G. Comparison of sodium and KCl-MgCl2 as heat transfer fluids in CSP solar tower with sCO2 power cycles. *Sol. Energy* **2018**, *162*, 510−524.

(13) Ruh, A.; Spiegel, M. Thermodynamic and kinetic consideration on the corrosion of Fe, Ni and Cr beneath a molten KCl−ZnCl2 mixture. *Corros. Sci.* **2006**, *48* (3), 679−695.
(14) Olson, L. C.; Ambrosek, J. W.; Sridharan, K.; Anderson, M. H.; Allen, T. R. Materials corrosion in molten LiF−NaF−KF salt. *J. Fluorine Chem.* **2009**, *130* (1), 67−73.
(15) Keiser, J. *Compatibility Studies of Potential Molten-Salt Breeder Reactor Materials in Molten Fluoride Salts*; Oak Ridge National Laboratory: Oak Ridge, TN, 1977.
(16) Liu, M.; Zheng, J.; Lu, Y.; Li, Z.; Zou, Y.; Yu, X.; Zhou, X. Investigation on corrosion behavior of Ni-based alloys in molten fluoride salt using synchrotron radiation techniques. *J. Nucl. Mater.* **2013**, *440* (1−3), 124−128.
(17) Edeleanu, C.; Littlewood, R. Thermodynamics of corrosion in fused chlorides. *Electrochim. Acta* **1960**, *3* (3), 195−207.
(18) Keiser, J.; DeVan, J.; Manning, D. *Corrosion Resistance of Type 316 Stainless Steel to Li_2BeF_4*; Oak Ridge National Laboratory: Oak Ridge, TN, 1977.
(19) Keiser, J.; Manning, D.; Clausing, R. Corrosion Resistance of Some Nickel-Base Alloys to Molten Fluoride Salts Containing UF4 and Tellurium. *Proc. - Electrochem. Soc.* **1976**, *1976*, 315−328.
(20) Reed, T. B. *Free Energy of Formation of Binary Compounds*; MIT Press: Cambridge, MA, 1971.
(21) Manly, W.; Adamson, G., Jr; Coobs, J.; DeVan, J.; Douglas, D.; Hoffman, E.; Patriarca, P. *Aircraft Reactor Experiment—Metallurgical Aspects*; Oak Ridge National Laboratory: Oak Ridge, TN, 1958.
(22) Kondo, M.; Nagasaka, T.; Muroga, T.; Sagara, A.; Noda, N.; Xu, Q.; Ninomiya, D.; Masaru, N.; Suzuki, A.; Terai, T. High performance corrosion resistance of nickel-based alloys in molten salt flibe. *Fusion Sci. Technol.* **2009**, *56* (1), 190−194.
(23) Marecek, M.; Slama, P. Corrosion testing of nickel alloy for molten salt reactors. *J. Achievements Mater. Manuf. Eng.* **2015**, *70*, 78−85.
(24) Guo, S.; Zhang, J.; Wu, W.; Zhou, W. Corrosion in the molten fluoride and chloride salts and materials development for nuclear applications. *Prog. Mater. Sci.* **2018**, *97*, 448−487.
(25) Zhang, J.; Forsberg, C. W.; Simpson, M. F.; Guo, S.; Lam, S. T.; Scarlat, R. O.; Carotti, F.; Chan, K. J.; Singh, P. M.; Doniger, W.; Sridharan, K.; Keiser, J. R. Redox potential control in molten salt systems for corrosion mitigation. *Corros. Sci.* **2018**, *144*, 44−53.
(26) Ludwig, D.; Olson, L.; Sridharan, K.; Anderson, M.; Allen, T. High temperature electrochemistry of molten fluoride salt for measurement of dissolved chromium. *Corros. Eng., Sci. Technol.* **2011**, *46* (4), 360−364.
(27) Phillips, J.; Gale, R.; Wier, R.; Osteryoung, R. Glassy carbon rotating ring-disc electrode for molten salt studies. *Anal. Chem.* **1976**, *48* (8), 1266−1268.
(28) Sona, C. S.; Gajbhiye, B. D.; Hule, P. V.; Patwardhan, A. W.; Mathpati, C. S.; Borgohain, A.; Maheshwari, N. K. High temperature corrosion studies in molten salt-FLiNaK. *Corros. Eng., Sci. Technol.* **2014**, *49* (4), 287−295.
(29) Patel, N. S.; Pavlík, V.; Kubíková, B.; Nosko, M.; Danielik, V.; Boča, M. Corrosion behaviour of Ni-based superalloys in molten FLiNaK salts. *Corros. Eng., Sci. Technol.* **2019**, *54* (1), 46−53.
(30) Raiman, S. S.; Sulejmanovic, D.; Utlak, S.; Kurley, J., III; Ponder, W. S.; Mcmurray, J. W.; Pint, B. A. *Corrosion of 316H Stainless Steel in Molten NaCl-$MgCl_2$ With and Without Mg as a Redox Control Additive*; Oak Ridge National Laboratory: Oak Ridge, TN, 2019.
(31) Olson, L.; Sridharan, K.; Anderson, M.; Allen, T. Intergranular corrosion of high temperature alloys in molten fluoride salts. *Mater. High Temp.* **2010**, *27* (2), 145−149.
(32) Fukumoto, K.-i.; Fujimura, R.; Yamawaki, M.; Arita, Y. Corrosion behavior of Hastelloy-N alloys in molten salt fluoride in Ar gas or in air. *J. Nucl. Sci. Technol.* **2015**, *52* (10), 1323−1327.
(33) Raiman, S. S.; Lee, S. Aggregation and data analysis of corrosion studies in molten chloride and fluoride salts. *J. Nucl. Mater.* **2018**, *511*, 523−535.
(34) Pint, B. A.; McMurray, J. W.; Willoughby, A. W.; Kurley, J. M.; Pearson, S. R.; Lance, M. J.; Leonard, D. N.; Meyer, H. M.; Jun, J.; Raiman, S. S.; Mayes, R. T. Re-establishing the paradigm for evaluating halide salt compatibility to study commercial chloride salts at 600° C−800° C. *Mater. Corros.* **2019**, *70*, 1439.
(35) Ouyang, F.-Y.; Chang, C.-H.; You, B.-C.; Yeh, T.-K.; Kai, J.-J. Effect of moisture on corrosion of Ni-based alloys in molten alkali fluoride FLiNaK salt environments. *J. Nucl. Mater.* **2013**, *437* (1−3), 201−207.
(36) Indacochea, J. E.; Smith, J. L.; Litko, K. R.; Karell, E. J. Corrosion performance of ferrous and refractory metals in molten salts under reducing conditions. *J. Mater. Res.* **1999**, *14* (5), 1990−1995.
(37) Indacochea, J. E.; Smith, J. L.; Litko, K. R.; Karell, E. J.; Rarez, A. G. High-Temperature Oxidation and Corrosion of Structural Materials in Molten Chlorides. *Oxid. Met.* **2001**, *55* (1), 1−16.
(38) Sridharan, K.; Allen, T., Corrosion in molten salts. In *Molten Salts Chemistry*; Elsevier: 2013; pp 241−267.
(39) Ye, X.-X.; Ai, H.; Guo, Z.; Huang, H.; Jiang, L.; Wang, J.; Li, Z.; Zhou, X. The high-temperature corrosion of Hastelloy N alloy (UNS N10003) in molten fluoride salts analysed by STXM, XAS, XRD, SEM, EPMA, TEM/EDS. *Corros. Sci.* **2016**, *106*, 249−259.
(40) Liu, S.; Liu, Z.; Wang, Y.; Tang, J. A comparative study on the high temperature corrosion of TP347H stainless steel, C22 alloy and laser-cladding C22 coating in molten chloride salts. *Corros. Sci.* **2014**, *83*, 396−408.
(41) Kelly, J. E. Generation IV International Forum: A decade of progress through international cooperation. *Prog. Nucl. Energy* **2014**, *77*, 240−246.
(42) Nelson, G. J.; Harris, W. M.; Lombardo, J. J.; Izzo, J. R.; Chiu, W. K.S.; Tanasini, P.; Cantoni, M.; Van herle, J.; Comninellis, C.; Andrews, J. C.; et al. Comparison of SOFC cathode microstructure quantified using X-ray nanotomography and focused ion beam−scanning electron microscopy. *Electrochem. Commun.* **2011**, *13* (6), 586−589.
(43) Volkovich, V. A.; Danilov, D. A.; Polovov, I. B.; Vasin, B. D.; Griffiths, T. R.; Aleksandrov, D. E.; Tropin, O. A.; Tsarevskii, D. V. Speciation of molybdenum and tungsten in molten chlorides: a spectroelectrochemical study. *ECS Trans.* **2006**, *3* (35), 555−566.
(44) Ivanov, A.; Volkovich, V.; Poskryakov, D.; Vasin, B.; Griffiths, T. Electrode potentials of tungsten in fused alkali chlorides. In *AIP Conference Proceedings*; AIP Publishing: Melville, NY, 2016; p 020010.
(45) Sun, H.; Zhang, P.; Wang, J. Effects of alloying elements on the corrosion behavior of Ni-based alloys in molten NaCl-KCl-MgCl2 salt at different temperatures. *Corros. Sci.* **2018**, *143*, 187−199.
(46) Ding, W.; Shi, H.; Jianu, A.; Xiu, Y.; Bonk, A.; Weisenburger, A.; Bauer, T. Molten chloride salts for next generation concentrated solar power plants: Mitigation strategies against corrosion of structural materials. *Sol. Energy Mater. Sol. Cells* **2019**, *193*, 298−313.
(47) Gaskell, D. R.; Laughlin, D. E. *Introduction to the Thermodynamics of Materials*; CRC Press: Boca Raton, FL, 2017.
(48) Zhao, C.; Wada, T.; De Andrade, V.; Gürsoy, D.; Kato, H.; Chen-Wiegart, Y.-c. K. Imaging of 3D morphological evolution of nanoporous silicon anode in lithium ion battery by X-ray nano-tomography. *Nano Energy* **2018**, *52*, 381−390.
(49) Wittstock, A.; Zielasek, V.; Biener, J.; Friend, C.; Bäumer, M. Nanoporous gold catalysts for selective gas-phase oxidative coupling of methanol at low temperature. *Science* **2010**, *327* (5963), 319−322.
(50) Snyder, J.; Fujita, T.; Chen, M.; Erlebacher, J. Oxygen reduction in nanoporous metal−ionic liquid composite electro-catalysts. *Nat. Mater.* **2010**, *9* (11), 904.
(51) Erlebacher, J.; Aziz, M. J.; Karma, A.; Dimitrov, N.; Sieradzki, K. Evolution of nanoporosity in dealloying. *Nature* **2001**, *410* (6827), 450−453.
(52) Chen, Q.; Sieradzki, K. Spontaneous evolution of bicontinuous nanostructures in dealloyed Li-based systems. *Nat. Mater.* **2013**, *12* (12), 1102−1106.
(53) Chen-Wiegart, Y.-c. K.; Wang, S.; Lee, W.-K.; McNulty, I.; Voorhees, P. W.; Dunand, D. C. In situ imaging of dealloying during

https://dx.doi.org/10.1021/acsami.9b19099
ACS Appl. Mater. Interfaces 2020, 12, 17321−17333

nanoporous gold formation by transmission X-ray microscopy. *Acta Mater.* **2013**, *61* (4), 1118−1125.
(54) Wada, T.; Yubuta, K.; Inoue, A.; Kato, H. Dealloying by metallic melt. *Mater. Lett.* **2011**, *65* (7), 1076−1078.
(55) McCue, I.; Gaskey, B.; Geslin, P. A.; Karma, A.; Erlebacher, J. Kinetics and morphological evolution of liquid metal dealloying. *Acta Mater.* **2016**, *115*, 10−23.
(56) Geslin, P. A.; McCue, I.; Gaskey, B.; Erlebacher, J.; Karma, A. Topology-generating interfacial pattern formation during liquid metal dealloying. *Nat. Commun.* **2015**, *6*, 8887.
(57) Zhao, C.; Kisslinger, K.; Huang, X.; Lu, M.; Camino, F.; Lin, C.-H.; Yan, H.; Nazaretski, E.; Chu, Y.; Ravel, B. Bi-continuous pattern formation in thin films via solid-state interfacial dealloying studied by multimodal characterization. *Mater. Horiz.* **2019**, *6*, 1991.
(58) Wada, T.; Yubuta, K.; Kato, H. Evolution of a bicontinuous nanostructure via a solid-state interfacial dealloying reaction. *Scr. Mater.* **2016**, *118*, 33−36.
(59) Raiman, S. S.; Muralidharan, G.; Mayes, R.; Kurley, J., III. *Compatibility Studies of Cladding Candidates and Advanced Low-Cr Superalloys in Molten NaCl-$MgCl_2$*; Oak Ridge National Laboratory: Oak Ridge, TN, 2019.
(60) van der Marck, S. C. Percolation thresholds and universal formulas. *Phys. Rev. E: Stat. Phys., Plasmas, Fluids, Relat. Interdiscip. Top.* **1997**, *55* (2), 1514−1517.
(61) Geng, K.; Sieradzki, K. Dealloying at High Homologous Temperature: Morphology Diagrams. *J. Electrochem. Soc.* **2017**, *164* (6), C330−C337.
(62) Liu, S.; Ye, X.-X.; Jiang, L.; Cui, C.; Li, Z.; Huang, H.; Leng, B.; Zhou, X. Effect of tungsten content on the microstructure and tensile properties of Ni−xW−6Cr alloys. *Mater. Sci. Eng., A* **2016**, *655*, 269−276.
(63) Ai, H.; Ye, X.-X.; Jiang, L.; Leng, B.; Shen, M.; Li, Z.; Jia, Y.; Wang, J.-Q.; Zhou, X.; Xie, Y.; Xie, L. On the possibility of severe corrosion of a Ni-W-Cr alloy in fluoride molten salts at high temperature. *Corros. Sci.* **2019**, *149*, 218−225.
(64) Dolzhnikov, D.; Dai, S. *M4FT: 18OR110102182—Develop a New Composite Molten Salt Fluid Exhibiting an Increased Heat Capacity of 10%*; Oak Ridge National Laboratory: Oak Ridge, TN, 2018.
(65) Ge, M.; Coburn, D. S.; Nazaretski, E.; Xu, W.; Gofron, K.; Xu, H.; Yin, Z.; Lee, W.-K. One-minute nano-tomography using hard X-ray full-field transmission microscope. *Appl. Phys. Lett.* **2018**, *113* (8), No. 083109.
(66) Kaira, C. S.; Kantzos, C.; Williams, J. J.; De Andrade, V.; De Carlo, F.; Chawla, N. Microstructural evolution and deformation behavior of Al-Cu alloys: A Transmission X-ray Microscopy (TXM) and micropillar compression study. *Acta Mater.* **2018**, *144*, 419−431.
(67) Ye, S.; Chen, Z.; Ha, Y.-C.; Wiley, B. J. Real-Time Visualization of Diffusion-Controlled Nanowire Growth in Solution. *Nano Lett.* **2014**, *14* (8), 4671−4676.
(68) Li, L.; Chen-Wiegart, Y.-C. K.; Wang, J.; Gao, P.; Ding, Q.; Yu, Y.-S.; Wang, F.; Cabana, J.; Wang, J.; Jin, S. Visualization of electrochemically driven solid-state phase transformations using operando hard X-ray spectro-imaging. *Nat. Commun.* **2015**, *6* (1), 6883.
(69) Pardoe, G.; Butler, E.; Gelder, D. Rapid quenching by the Taylor wire technique. *J. Mater. Sci.* **1978**, *13* (4), 786−790.
(70) Stull, D. R. Vapor pressure of pure substances. Organic and inorganic compounds. *Ind. Eng. Chem.* **1947**, *39* (4), 517−540.
(71) Xu, X.; Wang, X.; Li, P.; Li, Y.; Hao, Q.; Xiao, B.; Elsentriecy, H.; Gervasio, D. Experimental Test of Properties of KCl−MgCl2 Eutectic Molten Salt for Heat Transfer and Thermal Storage Fluid in Concentrated Solar Power Systems. *J. Sol. Energy Eng.* **2018**, *140* (5), No. 051011.
(72) Miao, J. W.; Charalambous, P.; Kirz, J.; Sayre, D. Extending the methodology of X-ray crystallography to allow imaging of micro-metre-sized non-crystalline specimens. *Nature* **1999**, *400* (6742), 342−344.
(73) Schindelin, J.; Arganda-Carreras, I.; Frise, E.; Kaynig, V.; Longair, M.; Pietzsch, T.; Preibisch, S.; Rueden, C.; Saalfeld, S.; Schmid, B.; Tinevez, J.-Y.; White, D. J.; Hartenstein, V.; Eliceiri, K.; Tomancak, P.; Cardona, A. Fiji: an open-source platform for biological-image analysis. *Nat. Methods* **2012**, *9*, 676.

https://dx.doi.org/10.1021/acsami.9b19099
ACS Appl. Mater. Interfaces 2020, 12, 17321−17333